A new system for measuring the photochemical ozone production rate in the atmosphere

A new system for measuring the photochemical ozone production rate in the atmosphere

Journal:	*Environmental Science & Technology*
Manuscript ID	es-2016-04639k.R2
Manuscript Type:	Article
Date Submitted by the Author:	n/a

Complete List of Authors:	Sadanaga, Yasuhiro; Osaka Prefecture University, Applied Chemistry Kawasaki, Shio; Osaka Prefecture University, Applied Chemistry Tanaka, Yuki; Osaka Prefecture University, Applied Chemistry; Kyoto University, Institute of Chemical Research Kajii, Yoshizumi; Kyoto University, Graduate School of Global Environmental Studies; National Institute for Environmental Studies Bandow, Hiroshi; Graduate School of Engineering, Osaka Prefecture University, Department of Applied Chemistry

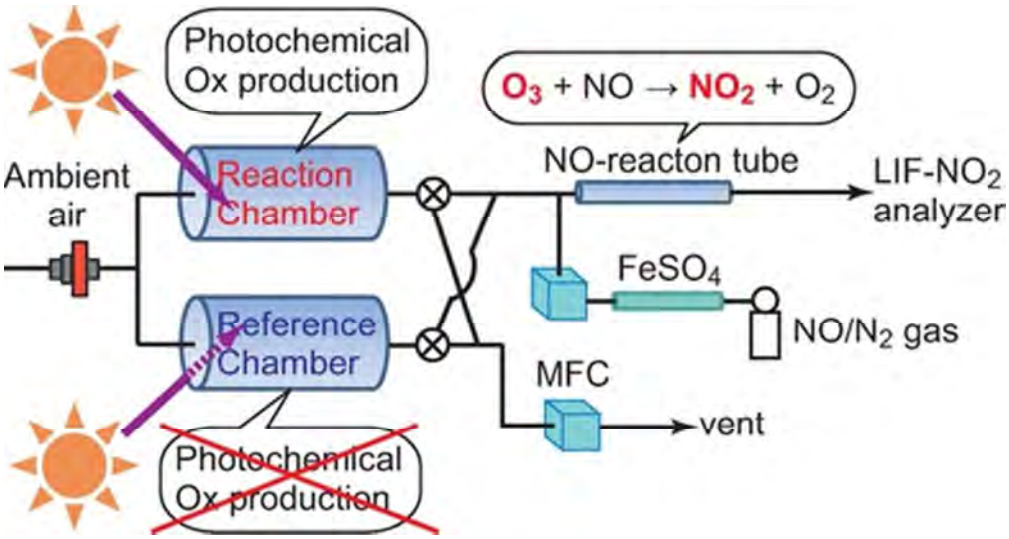

TOC/Abstract art

43x22mm (300 x 300 DPI)

A new system for measuring the photochemical ozone production rate in the atmosphere

Yasuhiro Sadanaga[1*], Shio Kawasaki[1], Yuki Tanaka[1,2], Yoshizumi Kajii[3,4], and Hiroshi Bandow[1]

1. Department of Applied Chemistry, Graduate school of Engineering, Osaka Prefecture University, 1-1 Gakuen-cho, Naka-ku, Sakai, Osaka 599-8531, Japan.
2. Now at Institute of Chemical Research, Kyoto University, Gokasho, Uji, Kyoto 611-0011, Japan.
3. Graduate School of Global Environmental Studies, Kyoto University, Yoshida-Nihonmatsu-cho, Sakyo-ku, Kyoto, Kyoto 606-8316, Japan.
4. National Institute for Environmental Studies, 16-2 Onogawa, Tsukuba, Ibaraki 305-8506, Japan.

* Corresponding author:
E-mail: sadanaga@chem.osakafu-u.ac.jp
tel: +81-72-254-9326
fax: +81-72-254-9325

Abstract

We have developed a new system for measuring photochemical ozone production rates in the atmosphere. Specifically, the system measures the net photochemical oxidant (O_x: the sum of ozone (O_3) and nitrogen dioxide (NO_2)) production rates ($P-L(O_x)$). Measuring O_x avoids issues from perturbations to the photostationary states between nitrogen oxides (NO_x) and O_3. This system has "reaction" and "reference" chambers. Ambient air is introduced into both chambers and O_x is photochemically-produced in the reaction chamber and not generated in the reference chamber. Air from the chambers is alternately introduced into an NO-reaction (NO: nitric oxide) tube to convert O_3 to NO_2, and then the O_x concentration is measured as NO_2 using a laser-induced fluorescence technique. $P-L(O_x)$ was obtained by dividing the difference in O_x concentrations between air samples from the two chambers by the mean residence time of the air in the reaction chamber. In this study, the $P-L(O_x)$ measurement system was characterized and the current detection limit of $P-L(O_x)$ was determined to be 0.54 ppbv h^{-1} with an integration time of 60 s (S/N=2), assuming an ambient O_x concentration of 100 ppbv. Field measurements of $P-L(O_x)$ were conducted using the system at a remote forest location.

Keywords

Production rate; Oxidant; Ozone; Laser-induced fluorescence

1. Introduction

Tropospheric ozone (O_3) is a harmful air pollutant in the atmosphere and a key component in the production of photochemical smog. Ozone hinders the growth of plants,[1,2] and is responsible for numerous health problems, such as respiratory illnesses.[3−5] Ozone is also an important greenhouse gas that contributes to climate change.[6] Appropriate ozone control strategies are required to improve regional and global air quality.

Tropospheric ozone is generated through reactions involving nitrogen oxides (NO_x: the sum of nitric oxide (NO) and nitrogen dioxide (NO_2)) and volatile organic compounds (VOCs) in the presence of solar ultraviolet (UV) light. Tropospheric ozone is generated in the photolysis of NO_2:

$$NO_2 + h\nu\,(\lambda < 420\ \text{nm}) \rightarrow NO + O(^3P), \quad (1)$$

$$O(^3P) + O_2 + M \rightarrow O_3 + M, \quad (2)$$

where M is a third-body molecule such as N_2 and O_2 in the atmosphere. The inverse of reactions (1) and (2) regenerates NO_2 and destroys ozone:

$$NO + O_3 \rightarrow NO_2 + O_2. \quad (3)$$

Photochemical ozone production in the troposphere is substantially controlled by the reaction of NO with peroxy radicals (RO_2; R means an organic group):

$$RO_2 + NO \rightarrow RO + NO_2, \quad (4)$$

$$RO + O_2 \rightarrow HO_2 + \text{carbonyl compounds}, \quad (5)$$

$$HO_2 + NO \rightarrow OH + NO_2. \quad (6)$$

Peroxy radicals are produced by the reaction of OH radicals with VOCs and CO:

$$OH + VOCs \rightarrow R + H_2O, \quad (7)$$

$$R + O_2 + M \rightarrow RO_2 + M, \quad (8)$$

$$OH + CO \rightarrow H + CO_2, \quad (9)$$

$$H + O_2 + M \rightarrow HO_2 + M. \quad (10)$$

Reactions (4)−(10) form a chain reaction centered on OH, HO_2 and RO_2 radicals to generate tropospheric ozone. VOCs act as a propagator of the chain reaction. NO_x act as both a propagator and a terminator of the chain reaction while NO_x is the direct precursor of ozone. NO_2 reacts with OH to generate nitric acid, which is a termination reaction of the chain reaction:

$$OH + NO_2 + M \rightarrow HNO_3 + M. \quad (11)$$

Hence the relationship between ozone formation and precursor concentrations is non-linear and complex. An example of the complexity is the ozone production regime, which consists of "NO_x-limited" and "VOC-limited" (or NO_x-saturated) regimes.[7,8] Ozone production rates increase with NO_x increases in a NO_x-limited regime, while ozone production rates increase with VOCs in a VOC-limited regime. Ozone production rates do not significantly increase with increased VOC concentrations under NO_x-limited regimes, while ozone production rates decrease when NO_x concentrations increase under VOC-limited regimes. Qualitative relationships between NO_x-limited and VOC-limited regimes can be described using empirical kinetic modelling approach (EKMA) diagrams and the VOC/NO_x ratio is an important factor for determining the ozone production regime.[9] Despite the ozone formation process being well-understood, the quantitative relationship between precursors is not sufficiently understood, even though a number of studies have focused on this issue.[10−13] Highlighting the importance of this issue, ozone concentrations are still increasing, despite a decrease in the concentrations of NO_x and VOCs in some regions.[14] One of the aspects hindering quantitative understanding of the relationship between ozone and its precursors is that there are many different VOC species. Lewis et al.[15] identified more than 500 VOCs in urban air using double-column gas chromatography. The ozone production potential of VOCs varies according to the individual VOC and it is difficult to quantitatively estimate ozone production rates through considering the contribution of all VOCs in the atmosphere.

The ozone budget in the boundary layer can be expressed using Equation 12:[16]

$$\frac{\partial[\mathrm{O_3}]}{\partial t} = P - L(\mathrm{O_3}) - \frac{u_\mathrm{d}}{H}[\mathrm{O_3}] - \nabla \cdot ([\mathrm{O_3}]\boldsymbol{v}), \quad (12)$$

where $P-L(O_3)$, u_d, H and $\boldsymbol{v}$ are the net photochemical ozone production rate, ozone deposition velocity, mixing layer height, and wind velocity, respectively. Ozone concentration variations are affected by meteorological factors such as deposition, advection and vertical mixing, as well as chemical factors such as photochemical ozone production and loss. It is more difficult to evaluate the relationship between ozone and its precursors when considering meteorological factors alongside chemical factors when many different VOCs are present.

Recently, a system for directly measuring the photochemical ozone production rate in the atmosphere, the Measurement of Ozone Production Sensor (MOPS), has been developed.[17] This system can separate chemical and meteorological factors responsible for ozone concentration variations and significantly improve understanding of photochemical ozone production. In the MOPS, ambient air is introduced into two chambers, a UV-transparent (reaction) and a UV protection (reference) chamber in the presence of solar UV light. Ozone is produced photochemically in the reaction chamber and not formed in the reference chamber. $P-L(O_3)$ is obtained from the difference between O_3 concentrations in the reaction and reference chambers. The system does not measure O_3 concentrations directly; it measures combined ozone and NO_2 concentrations (abbreviated as O_x). This is because the photostationary states between NO_x and O_3 are different in the reaction and reference chambers, producing variations in ozone concentrations. During the daytime, NO_x and O_3 rapidly form the photostationary state described by reactions (1)−(3). The reaction rate (1) in the reference chamber is slower than that in the reaction chamber. Reaction (3) dominates in the reference chamber and O_3 concentrations decrease accordingly. As a result, $P-L(O_3)$ is overestimated in this scenario. The O_x concentration is constant during reactions (1)–(3), so measuring the net photochemical O_x production rates ($P-L(O_x)$) is more practical than measuring $P-L(O_3)$. $P-L(O_x)$ has been measured in the urban

atmosphere using the MOPS.[16,18] The MOPS would be a revolutionary instrument for understanding ozone budgets, but further improvements to it are required. For example, wall losses of NO_2 in the chamber under humid conditions are problematic[17,18]. Also, the O_x detection system could be improved. In the MOPS, O_x concentrations are measured by the photolytic conversion of NO_2 to O_3, followed by O_3 detection by an O_3 analyzer using the UV-absorption method. The O_x detection system is simple, but the conversion efficiency of NO_2 to O_3 is not 100% and depends on NO_x and O_3 concentrations. This conversion efficiency dependence creates additional uncertainty in the $P-L(O_x)$ measurements. In addition, the response of the O_3 analyzer to changes in temperature and relative humidity causes the uncertainty[18].

We have developed a new system for measuring $P-L(O_x)$ in the atmosphere. In this article, the instrumentation used and characterization of the $P-L(O_x)$ measurement system are described. We also conducted a field study involving $P-L(O_x)$ measurements in a remote forest area and the results of the field study are briefly discussed. In this system, O_x concentrations are measured by conversion of O_3 to NO_2 using a large excess of NO, followed by NO_2 detection using an NO_2 analyzer applying laser-induced fluorescence (LIF). The conversion efficiency of O_3 to NO_2 was almost 100% and was independent of O_3 concentrations. These modifications enable more accurate O_x measurements. Wall losses of NO_2 and O_3 in the chamber were negligible in this instrument, so that absolute uncertainties of the $P-L(O_x)$ measurements can be reduced.

2. Instrumentation

2.1. Overview

Figure 1 presents a schematic of the $P-L(O_x)$ measurement system. The system features reaction and reference chambers with identical dimensions (inner volume of 11.5 L) made of quartz and Pyrex, respectively. The outer wall of the reference chamber was coated with a UV protection film

so that photochemical reactions could not occur. Both chambers can be directly exposed to sunlight outdoors and ambient air is introduced into both chambers. Photochemical reactions then proceed to generate O_x in the reaction chamber, while O_x is not generated in the reference chamber. A Teflon filter was set before the chambers to remove particles. Air passed through the reaction and reference chambers is then alternately introduced into an NO reaction tube every 2 minutes to covert O_3 to NO_2 in the presence of a high concentration of NO. The O_x concentration, as NO_2, is then measured using LIF. Gas flow from the reaction or reference chambers to the LIF-NO_2 analyzer via the NO-reaction tube was switched using two Teflon three-way solenoid valves (FSS-0306YN; Flon Industry) located just before the NO-reaction tube (see Figure 1). The increment of O_x (ΔO_x) is defined as the difference in O_x concentrations between the reaction and reference chambers. $P-L(O_x)$ is obtained by dividing ΔO_x by the mean residence time of air in the reaction chamber ($\langle \tau \rangle$) (Equation 13).

$$P - L(O_x) = \frac{\Delta O_x}{\langle \tau \rangle} \quad (13)$$

The air flow from the chambers that is not introduced into the NO-reaction tube was evacuated by a diaphragm pump to avoid undesirably stacking the air flow in the chambers. The evacuated flow rate is controlled by a mass flow controller and the flow rates in the reaction and reference chambers were always the same.

2.2. Reaction and reference chambers

Figure 2 presents a schematic diagram of the reaction chamber, which consists of a quartz cylinder, two quartz windows, and aluminum flanges to connect the quartz cylinder to the quartz windows. The length and inner diameter of the quartz cylinder are 500 and 171 mm, respectively. The quartz window has a quartz tube (outer diameter of 12.7 mm) for air intake and outflow. For air intake, the quartz tube passes through one quartz window and is bent into an L-shape at the inner surface side

of the quartz window (see Figure 2). The other quartz window is equipped with a straight quartz tube for air outflow (see Figure 2). The reason for this configuration is explained in detail in Section 3.3. The quartz windows for air intake and outflow are referred to as “L-shape” and “straight”, respectively, in the rest of this article. The inner wall of the reaction chamber (i.e. quartz cylinder and windows) was coated with a clear Teflon film (TC-20; Yoshida SKT) to avoid wall losses (see Section 3.4). The specifications of the reference chamber were almost the same as those of the reaction chamber, but a cylinder and two windows are made of Pyrex. The inner wall of the reference chamber (i.e. Pyrex cylinder and windows) was also coated with a clear Teflon film. Also, the outer wall of the reference chamber was coated with a UV protection film (SH2CLAR; 3M).

Light transmittance through the clear Teflon and UV protection films was measured using a commercially available UV-Visible spectrophotometer (V-630; JASCO Corporation) with a spectral resolution of 1 nm. The light sources for the spectrophotometer are deuterium and halogen lamps for UV and visible regions, respectively. Two synthetic quartz plates were prepared and one side of the plate was coated with the clear Teflon or UV protection film. Figure 3 shows transmission spectra of the quartz plates coated with clear Teflon and UV protection films. Light transmittance through the clear Teflon film was more than 99.8% at wavelengths longer than 280 nm, highlighting that solar UV had no trouble penetrating the clear Teflon film. For the UV protection film, the half cut-off wavelength was measured to be 405 nm and light transmittance was near zero at wavelengths less than 390 nm. We also investigated solar UV transmittance through the reaction and reference chambers using natural sunlight. The results of these experiments are described in Section 3.2.

2.3. NO-reaction tube

A PFA tube (outer diameter of 12.7 mm; inner diameter of 10.7 mm; length of 44 cm) was used as a NO-reaction tube. Sample air was introduced into the NO-reaction tube and was immediately

mixed with NO/N_2 gas (Taiyo Nissan, 98.8 ppmv NO (ppmv = parts per million by volume)) using a PFA Union Tee (Swagelok) to convert O_3 in the sample to NO_2. In advance, the NO/N_2 gas passed through a cylinder filled with powderized crystals of $FeSO_4 \cdot 7H_2O$ to reduce NO_2 in the NO/N_2 gas cylinder to NO.[19] The flow rate of the NO/N_2 gas was maintained at 10 cm^3 min^{-1} using a mass flow controller (3660; KOFLOC). The total flow rate of the reaction mixture in the NO-reaction tube was controlled by the flow rate of the LIF-NO_2 analyzer and was measured to be 553 cm^3 min^{-1} using a bubble film flow meter (Gilibrator 2; Sensidyne).

A high concentration of NO (1.79 ppmv) exists in the NO-reaction tube. We evaluated the effect of the reaction of NO_2 with NO to produce N_2O_3, which might influence an NO_2 concentration in the reaction tube and accuracy of the $P-L(O_x)$ measurement. This reaction is an equilibrium reaction and the equilibrium constant is 2.10 x 10^{-20} cm^3 $molecule^{-1}$ s^{-1} at 298 K.[20] Assuming that NO and NO_2 concentrations are 1.79 ppmv and 100 ppbv, respectively, the N_2O_3 concentration is calculated to be 2.28 x 10^6 molecules cm^{-3} (0.093 pptv), which is extremely low concentration. We concluded that the reaction $NO_2 + NO \rightarrow N_2O_3$ is negligible as an NO_2 sink in the NO-reaction tube.

2.4. NO_2 measurement using laser-induced fluorescence

NO_2 concentrations were measured using LIF. Detailed descriptions of the technique and instrumentation used have been reported previously.[21,22] Briefly, ambient air was introduced into the fluorescence detection cell through an orifice (0.254 mm diameter). A second harmonic of a solid-state pulsed Nd:YAG laser (Awave-532nm-8W-10kHz; Advanced Optowave) was produced to excite NO_2 molecules in the detection cell. The Nd:YAG laser had a frequency of 10 kHz, pulse width of 76 ns, beam diameter of 1 mm and maximum output of 7 W. Fluctuations in laser power were monitored outside the detection cell using a photodiode (S1226-5BQ; Hamamatsu) to correct the sensitivity of the LIF system as fluctuations in laser power occurred. The cell was maintained under vacuum using a

rotary pump (RV8; Edwards) to decrease quenching of excited NO_2 molecules. Pressure in the cell was approximately 330 hPa and was measured using a capacitance manometer (Model 720; Setra).

Fluorescence was focused onto a photocathode of a dynode-gated photomultiplier tube (R928P; Hamamatsu) through two lenses and a sharp cut-off filter (R62; Asahi Technoglass), which was used to cut off scattered light to the photomultiplier tube. The photomultiplier tube was time-gated to distinguish fluorescence from scattered light using a dynode gating system that was normally off (C1392-56; Hamamatsu). The gating system was controlled by a positive transistor-transistor logic (TTL) pulse that was generated from a delay/pulse generator (DG535; Stanford Research Systems). The negative output signal from the photomultiplier tube was passed to an amplification/discrimination unit (C9744; Hamamatsu) for conversion to positive TTL pulses. The number of these pulses during a single gate period was counted by a photon counting board (M8784; Hamamatsu) that was slotted into a master computer (Dimension 8250; Dell). Typical gate timing for photon counting ranged between 0.3 and 3.1 μs after the laser pulse. The detection limit of the NO_2-LIF instrument was estimated to be 0.053 ppbv (parts per billion by volume) at a signal-to-noise ratio (S/N) = 2 at an integration time of 60 s and laser power of 7 W (see Section 3.5)[21, 22].

3. Characterization of the instrument

3.1. Solar UV transmittance through glass walls of the reaction and reference chambers

HO_x (OH and HO_2) radicals play a central role in photochemical O_x production. HO_x radicals are initially generated by the photolysis of species such as ozone, nitrous acid and aldehydes. To obtain $P-L(O_x)$ with a high accuracy, solar UV transmittance through the reaction and reference chambers should be sufficiently high and low, respectively. To investigate solar UV transmittance through the reaction and reference chambers, the solar actinic fluxes in the reaction and reference chambers were measured using a spectroradiometer (Meteorologie Consult GmBH, Germany). Details of the

spectroradiometer have previously been described by Kanaya et al.[23] and the same radiometer was used in this study. The solar actinic flux in ambient air was also measured for comparison. The measurements were conducted at noon on a sunny day (24 April 2014) on the roof of the B5 building at Osaka Prefecture University, Osaka, Japan.

Photolysis frequencies of NO_2 ($J(NO_2)$), O_3 ($J(O_3)$), HONO (J(HONO)) and HCHO (J(HCHO)) were calculated using their associated measured solar actinic fluxes. The calculation method used in this study is the same as that described by Kanaya et al.[23] It should be noted that $J(O_3)$ and J(HCHO) are the rate constants for reactions (14) and (15), respectively.

$$O_3 + h\nu \rightarrow O_2 + O(^1D), \quad (14)$$

$$HCHO + h\nu \rightarrow H + HCO. \quad (15)$$

Table 1 presents the $J(NO_2)$, $J(O_3)$, J(HONO) and J(HCHO) results for ambient air, and the reaction and reference chambers. Photolysis frequencies in the reaction chamber were in agreement with those measured in ambient air to within 3 %. Conversely, $J(O_3)$, J(HONO) and J(HCHO) in the reference chamber were less than 2 % of those in ambient air. These results indicate that the amount of solar UV light in the reaction chamber was nearly the same as that in ambient air and HO_x radical production was sufficiently suppressed in the reference chamber. $J(NO_2)$ in the reference chamber was 12% of that in ambient air. It is reasonable that $J(NO_2)$ did not completely diminish in the reference chamber because the half cut-off wavelength for the UV protection film was 405 nm (Section 2.2). It should be noted that $J(NO_2)$ is the rate constant for reaction (1) and does not contribute to photochemical O_x production.

3.2. O_3 to NO_2 conversion efficiency in the NO-reaction tube

Quantitative conversion of O_3 to NO_2 in the NO-reaction tube is crucial to measuring $P-L(O_x)$ accurately. The O_3 to NO_2 conversion efficiency (α) was investigated. O_3 was generated using a

low-pressure mercury lamp and the ozone concentration ($[O_3]_{UV}$) was measured using a commercially-available O_3 monitor based on the UV-absorption method (Model 1150; Dylec). A known concentration of ozone (ozone sample gas) was introduced into the NO-reaction tube for conversion to NO_2, followed by analysis using the LIF-NO_2 analyzer to measure the NO_2 concentration ($[NO_2]'_{LIF}$). The ozone concentrations were controlled within the range 12–158 ppbv. The flow rates of the ozone sample gas and the NO/N_2 gas introduced into the NO-reaction tube were 543 and 10 cm^3 min^{-1}, respectively, and the total flow rate in the NO-reaction tube was 553 cm^3 min^{-1}, which was controlled by the flow rate of the LIF-NO_2 analyzer as described in Section 2.3. It should be noted that the ozone concentration of the ozone sample gas was diluted and $[O_3]_{UV}$ decreased in the NO-reaction tube through addition of NO/N_2 gas. Therefore, the relationship between $[NO_2]'_{LIF}$ and $[O_3]_{UV}$ is described through Equation 16:

$$[NO_2]'_{LIF} = \frac{543}{553}[O_3]_{UV}\alpha . \quad (16)$$

Figure 4 presents the relationship between $[NO_2]_{LIF}$ and $[O_3]_{UV}$. $[NO_2]_{LIF}$ is the corrected concentration of NO_2 after dilution in the NO-reaction tube.

$$[NO_2]_{LIF} = \frac{553}{543}[NO_2]'_{LIF} . \quad (17)$$

The slope of the regression line in Figure 4 is the conversion efficiency.

$$[NO_2]_{LIF} = [O_3]_{UV}\alpha . \quad (18)$$

α was calculated to be 0.990 ± 0.006 (1σ), showing that complete conversion of O_3 to NO_2 in the NO-reaction tube was achieved when O_3 concentrations were less than 160 ppbv.

3.3. Mean residence time of air in the reaction chamber

The mean residence time of air in the reaction chamber ($\langle \tau \rangle$) is critical for calculating $P-L(O_x)$.

As the inner volume and airflow rate in the reaction chamber were 11.5 L and 543 cm^3 min^{-1}, respectively, the mean residence time was 21.1 minutes assuming complete plug flow. It should be noted that the airflow rate in the reaction chamber was obtained by subtracting the flow rate of the NO/N_2 gas introduced into the NO-reaction tube (10 cm^3 min^{-1}) from the flow rate of the LIF-NO_2 analyzer (553 cm^3 min^{-1}).

$\langle\tau\rangle$ was determined experimentally since the actual flow in the reaction chamber would not be the same as the plug flow. A short pulse of NO_2 gas (ca.10 ppmv) was introduced into the reaction chamber at $\tau = 0$ and the time profile of NO_2 concentrations ($C(\tau)$) at the exit of the chamber was measured using the LIF-NO_2 analyzer. The pulse width of the introduced NO_2 gas was approximately 10 s and was sufficiently shorter than $\langle\tau\rangle$. The flow rate in the reaction chamber was controlled to be 543 cm^3 min^{-1} by adding zero air at a rate of 10 cm^3 min^{-1} between the exit of the chamber and the LIF-NO_2 analyzer. $C(\tau)$ was converted into the probability density function ($E(\tau)$) by normalizing $C(\tau)$ using Equation 19.

$$E(\tau) = \frac{C(\tau)}{\int_0^\infty C(\tau)d\tau}. \quad (19)$$

$\langle\tau\rangle$ is an expectation value and was calculated using Equation 20.

$$\langle\tau\rangle = \int_0^\infty \tau E(\tau)d\tau. \quad (20)$$

Figure 5(a) presents an example time profile of $E(\tau)$ in the reaction chamber. The measurements were performed five times and $\langle\tau\rangle$ was calculated to be 20.5 ± 0.4 min, which was close to the value calculated assuming complete plug flow (21.1 min). Figure 5(a) also shows a fitting curve based on a lognormal distribution. The χ^2 value of the fitting curve was calculated to be 5.53 x 10^{-7} and the time profile of $E(\tau)$ followed a lognormal distribution.

Figure 5(b) presents an example of time profiles of $E(\tau)$ in the reaction chamber when a

294 "straight" quartz window was used for air intake. The measurements were performed five times and $\langle \tau \rangle$
295 was calculated to be 22.1 ± 0.5 min, which was also close to the value calculated assuming complete
296 plug flow. A large, sharp peak of $E(\tau)$ was observed at approximately 40 s and then $E(\tau)$ decreased
297 moderately, however. This was likely because the residence time of air around the central axis of the
298 quartz cylinder was extremely short. We suggest that $\langle \tau \rangle$ in the reaction chamber is further from the
299 actual reaction time when a "straight" quartz window is used for air intake. As such, an "L-shape"
300 quartz window was used for air intake.
301
302 **3.4. O_3 and NO_2 loss in the reaction and reference chambers**
303 Wall losses of O_3 and NO_2 decrease the accuracy of $P-L(O_x)$. Inner walls of both reaction and
304 reference chambers were coated with a clear Teflon film to avoid wall losses (Section 2.2).
305 To investigate wall losses of O_3, it was generated using a low-pressure mercury lamp and then
306 introduced into the chamber. O_3 concentrations before the air inlet ($[O_3]_{in}$) and after the air outlet
307 ($[O_3]_{out}$) of the chamber were measured using the NO_2-LIF instrument through the NO-reaction tube.
308 The chamber flow rate was maintained at 543 cm^3 min^{-1}. This experiment was performed under dark
309 condition. Figure 6 presents the relationship between $[O_3]_{in}$ and $[O_3]_{out}$ for the reaction and reference
310 chambers. Wall losses of O_3 were found to be approximately 10 % for both chambers without clear
311 Teflon coating. Wall losses decreased to less than 1.5 % when the chambers were coated with Teflon.
312 This finding shows that Teflon coating of the inner walls of the chambers is necessary to accurately
313 measure $P-L(O_x)$.
314 NO_2 wall losses were also investigated. NO_2 was generated using a gas-phase titration (GPT)
315 method and was introduced into the chamber. The details of the GPT method are described elsewhere.[23]
316 NO_2 concentrations before the air inlet ($[NO_2]_{in}$) and after the air outlet ($[NO_2]_{out}$) of the chamber were
317 measured using the NO_2-LIF instrument. The chamber flow rate was maintained at 543 cm^3 min^{-1}. The

measurements were performed under humid conditions because wall losses of NO_2 increase because of the reaction:

$$2NO_2 + H_2O(ads.) \rightarrow HNO_3 + HONO, \quad (21)$$

where H_2O(ads.) is a water molecule adsorbed on the surface of the inner wall. Humidity was measured using a chilled mirror dew point hygrometer (DPH-501B; Tokyo Opto-Electronics Co., Ltd.). The measurements were carried out under dry condition and relative humidity of about 80% (see Figure 7). The chambers with clear Teflon coatings were used in this experiment. This experiment was also performed under dark condition. Figure 7 presents the results of the comparison between $[NO_2]_{in}$ and $[NO_2]_{out}$ for the reaction and reference chambers. The measurements were performed three times for each experimental condition. The values of $[NO_2]_{out}$ were in agreement with $[NO_2]_{in}$ within one standard deviation under both dry and humidified conditions. We concluded that there were no significant wall losses of NO_2 in the chambers. Hence the use of glass chamber with clear Teflon coating improve wall loss effect of O_3 and NO_2 under dark condition.

Recently, HONO formation at the surface under illuminated condition has been proposed in the simulation chamber experiment,[24] and the HONO formation might affect photochemical O_x production in the reaction chamber. In addition, HCHO formation, ozone loss under humidified condition, and off-gassing of organic compounds at the surface[25] might influence photochemical O_x production in the reaction chamber. Evaluation of these factors might be an issue in the future in order to improve accuracy of the $P-L(O_x)$ measurement.

3.5. Detection limit and uncertainties of the instrument

The $P-L(O_x)$ detection limit ($P-L(O_x)_{min}$) using this instrument depends on the detection limit of the NO_2-LIF instrument ($[NO_2]_{min}$) and $\langle \tau \rangle$. Also, $P-L(O_x)$ is derived using ΔO_x, so the $P-L(O_x)_{min}$ also depends on the ambient O_x concentration ($[O_x]_{amb.}$). The $[NO_2]_{min}$ was estimated by the following

342 equation:

343 $$[\mathrm{NO_2}]_{\min} = \frac{S/N}{C\sqrt{P}}\sqrt{\frac{1}{m}+\frac{1}{n}}\frac{\sqrt{S_{\mathrm{BG}}}}{\sqrt{t}}, \quad (22)$$

344 where S/N is the signal to noise ratio at the detection limit, C is the NO_2 detection sensitivity (cps W^{-1}
345 $ppbv^{-1}$), P is the laser power (W), m and n are the numbers of fluorescence and background
346 measurement, respectively, S_{BG} is the background signal count rate (cps W^{-1}), and t is the integration
347 time (s). Under the typical condition, C and S_{BG} were measured to be 598 cps W^{-1} and 63.4 cps W^{-1}
348 $ppbv^{-1}$, respectively, and $[NO_2]_{min}$ was determined to be 0.053 ppbv at $S/N = 2$, $t = 60$ s, $m = n = 1$, and
349 $P = 7$ W.

350 For $P{-}L(O_x)_{min}$, background signal (S'_{BG}) is affected by $[O_x]_{amb.}$, that is, S'_{BG} is expressed by
351 the following formula:

352 $$S'_{\mathrm{BG}} = S_{\mathrm{BG}} + C[\mathrm{O_x}]_{\mathrm{amb.}}, \quad (23)$$

353 $P{-}L(O_x)_{min}$ can be estimated by the following equation:

354 $$P - L(\mathrm{O_x})_{\min} = \frac{S/N}{C\sqrt{P}}\sqrt{\frac{1}{m}+\frac{1}{n}}\frac{\sqrt{S_{\mathrm{BG}} + C[\mathrm{O_x}]_{\mathrm{amb.}}}}{\sqrt{t}}\frac{1}{\langle\tau\rangle}, \quad (24)$$

355 Hence $P{-}L(O_x)_{min}$ depends on ambient O_x concentrations. Assuming an ambient O_x concentration of 10,
356 50, and 100 ppbv, the detection limit of $P{-}L(O_x)$ was estimated to be 0.22, 0.39, and 0.54 ppbv h^{-1},
357 respectively, at $S/N = 2$, with an integration time of 60 s. It should be noted that the detection limit
358 estimated here is under the constant O_x concentration condition. The actual detection limit must be
359 higher than those values because there are natural O_x concentration variations in the atmosphere.

360 The main uncertainties associated with this instrument arise from $\langle\tau\rangle$[17] and the calibration of
361 the NO_2-LIF instrument. The uncertainty in $\langle\tau\rangle$ was estimated from the error associated with the
362 measurement of $\langle\tau\rangle$ (±4 %). The uncertainty in the calibration of the NO_2-LIF instrument was the same
363 as that of the LED-IF (light-emitting diode induced fluorescence) NO_2 analyzer[26] because the same

364 calibration system was used, and arises from NO calibration of the commercially-available NO_x
365 analyzer (±10 %) and NO_2 calibration using the GPT method (±10 %).[26]
366
367 **4. Atmospheric measurements**
368 Field measurements of $P-L(O_x)$ using this instrument were conducted at the Wakayama Forest
369 Research Station (WFRS), Kyoto University, Wakayama Prefecture, Japan, from 27 July, 2014, to 8
370 August, 2014. The WFRS was located at a latitude of 34.02°N, a longitude of 135.02°E, and an altitude
371 of 560 m above sea level. More details about the observatory are described elsewhere.[27] Briefly, the
372 observatory is located in a forested valley and there were no large industrial areas near it. The site is
373 about 35 km from the center of the city of Wakayama, which is the largest city in Wakayama Prefecture.
374 The site is in a remote area, but there are significant emissions of biogenic volatile organic
375 compounds.[24] Unfortunately, it was not sunny all day during the measurement period and O_3
376 concentrations peaked at approximately 10 ppbv over most of the study. NO_x concentrations were less
377 than 1 ppbv except when infrequent local emissions of NO_x from a nearby road were identified.
378 Figure 8 presents variations of $P-L(O_x)$, $J(NO_2)$, O_x and NO_x concentrations at WFRS from 5
379 to 7 August 2014. Unfortunately, most of the observation period were rainy days and we could measure
380 $P-L(O_x)$ for those three days only. $J(NO_2)$ was measured using the spectroradiometer described in
381 Section 3.1. O_3, NO and NO_2 concentrations were measured using commercially-available instruments
382 based on UV absorption (Model 49C; Thermo Electron), NO-O_3 chemiluminescence (Model 42i-TL;
383 Thermo Fisher Scientific) and cavity attenuated phase shift spectroscopy (CAPS-NO_2; Shoreline
384 Science Research Inc., licensed by Aerodyne Research Inc.) methods, respectively. $P-L(O_x)$ and O_x had
385 daytime maxima and nighttime minima for all days, indicating that O_x is photochemically produced
386 even in remote areas and under low NO_x and O_x concentrations. On 6 August, O_x concentrations
387 increased even though $P-L(O_x)$ values were almost 0 ppbv h^{-1} from 6:00 to 8:00. This result indicates

388 that the O_x increase was related to meteorological factors. Specifically, vertical mixing of air is weak at
389 night and O_3 concentrations near the ground's surface decreases because of processes like deposition.
390 The ground's surface is gradually warmed by sunlight in the morning and vertical mixing of air
391 resumes. Consequently, O_3 concentrations increase because of O_3 influx from above. $P-L(O_x)$ peaked
392 up to 10.5 ppbv h^{-1} around noon and photochemical O_3 production was active during the daytime.
393 However, O_x concentrations did not increase around noon. This suggests that O_3 increases through
394 photochemical production competed against O_3 decreases through non-photochemical factors such as
395 deposition, advection and reactions of O_3 with olefins.

396 Through the observation, we indicated that ozone can be produced photochemically, even in a
397 clean (i.e., low NO_x and O_x concentrations) environment. In addition, simultaneous measurements of
398 $P-L(O_x)$ and O_x concentrations can separate the factors of ozone concentrations variations, that is,
399 meteorological and photochemical factors. Observational researches of $P-L(O_x)$ are just beginning and
400 examples of the observations are still quite low. $P-L(O_x)$ measurements can simplify the tropospheric
401 ozone budget, and significantly improve understanding of ozone budget as described in Section 1.
402 Accumulation of $P-L(O_x)$ observations in the future must be useful in order to clarify photochemistry
403 and ozone budget in the troposphere.

404

405 **Acknowledgements**

406 The authors are grateful to Dr. Akira Ida, Mr. Ramasamy Sathiyamurthi (Kyoto University), Dr.
407 Hiroshi Tsurumaru (Kanazawa University) and Dr. Yoshihiro Nakashima (Tokyo University of
408 Agriculture and Technology) for their help with the measurements in Wakayama. This study was
409 supported by a Grant-in-Aid from the Japan Society for the Promotion of Science (Grant-in-Aid no.
410 23651018).

411

412 **References**

413 (1) Heath, R. L.; Lefohn, A. S.; Musselman, R. C. Temporal processes that contribute to nonlinearity in
414 vegetation responses to ozone exposure and dose. *Atmos. Environ.* **2009**, *43* (18), 2919−2928;
415 DOI: 10.1016/j.atmosenv.2009.03.011.
416 (2) Watanabe, M.; Matsuo, N.; Yamaguchi, M.; Matsumura, H.; Kohno, Y.; Izuta, T. Risk assessment of
417 ozone impact on the carbon absorption of Japanese representative conifers. *Eur. J. Forest Res.*
418 **2010**, *129* (3), 421−430; DOI: 10.1007/s10342-009-0316-0.
419 (3) Ho, W. C.; Hartley, W. R.; Myers, L.; Lin, M. H.; Lin, Y. S.; Lien, C. H.; Lin, R. S. Air pollution,
420 weather, and associated risk factors related to asthma prevalence and attack rate. *Environ. Res.*
421 **2007**, *104* (3), 402−409; DOI: 10.1016/j.envres.2007.01.007.
422 (4) Karakatsani, A.; Kapitsimadis, F.; Pipikou, M.; Chalbot, M. C.; Kavouras, I. G.; Orphanidou, D.;
423 Papiris, S.; Katsouyanni, K. Ambient air pollution and respiratory health effects in mail carriers.
424 *Environ. Res.* **2010**, *110* (3), 278−285; DOI: 10.1016/j.envres.2009.11.002.
425 (5) Neidell, M.; Kinney, P. L. Estimates of the association between ozone and asthma hospitalizations
426 that account for behavioral responses to air quality information. *Environ. Sci. Policy* **2010**, *13* (2),
427 97−103; DOI: 10.1016/j.envsci.2009.12.006.
428 (6) Myhre, G.; et al. Anthropogenic and Natural Radiative Forcing. *In Climate Change 2013: The*
429 *Physical Science Basis. Contribution of Working Group I to the Fifth Assessment Report of the*
430 *Intergovernmental Panel on Climate Change*; Stocker, T. F.; Qin, D.; Plattner, G. –K.; Tignor, M.;
431 Allen, S. K.; Boschung, J.; Nauels, A.; Xia, Y.; Bex, V.; Midgley, P. M., Eds.; Cambridge
432 University Press: New York 2008; pp 659−740.
433 (7) Milford, J. B.; Gao, D.; Sillman, S.; Blossey, P.; Russell, A. G. Total reactive nitrogen (NO_y) as an
434 indicator of the sensitivity of ozone to reductions in hydrocarbons and NO_x Emissions. *J. Geophys.*
435 *Res.* **1994**, *99* (D2), 3533−3542; DOI: 10.1029/93JD03224.

(8) Sillman, S. The relation between ozone, NO_x and hydrocarbons in urban and polluted rural environments. *Atmos. Environ.* **1999**, *33* (12), 1821−1845; DOI: 10.1016/S1352-2310(98)00345-8.

(9) Kinosian, J. R. Ozone-precursor relationships from EKMA diagrams. *Environ. Sci. Technol.* **1982**, *16* (12), 880−883; DOI: 10.1021/es00106a011.

(10) Kanaya, Y.; Fukuda, M.; Akimoto, H.; Takegawa, N.; Komazaki, Y.; Yokouchi, Y.; Koike, M.; Kondo, Y. Urban photochemistry in central Tokyo: 2. Rates and regimes of oxidant production. *J. Geophys. Res.* **2008**, *113* (D6), D06301, DOI:10.1029/2007JD008671.

(11) Sadanaga, Y.; Sengen, M.; Takenaka, N.; Bandow, H. Analyses of the ozone weekend effect in Tokyo, Japan: Regime of oxidant (O_3 + NO_2) production. *Aerosol Air Qual. Res.* **2012**, *12* (2), 161−168; DOI: 10.4209/aaqr.2011.07.0102.

(12) Chang, C. –Y.; Faust, E.; Hou, X.; Lee, P.; Kim, H. C.; Hedquist, B. C.; Liao, K. –J. Investigating ambient ozone formation regimes in neighboring cities of shale plays in the Northeast United States using photochemical modeling and satellite retrievals. *Atmos. Environ.* **2016**, *142*, 152−170; DOI: 10.1016/j.atmosenv.2016.06.058.

(13) Zou, Y.; Deng, X. J.; Zhu, D.; Gong, D. C.; Wang, H.; Li, F.; Tan, H. B.; Deng, T.; Mai, B. R.; Liu, X. T.; Wang, B. G. Characteristics of 1 year of observational data of VOCs, NO_x and O_3 at a suburban site in Guangzhou, China. *Atmos. Chem. Phys.* **2015**, *15* (12), 6625-6636; DOI: 10.5194/acp-15-6625-2015.

(14) Chou, C. C. −K.; Liu, S. C.; Lin, C. Y.; Shiu, C. J.; Chang, K. H. The trend of surface ozone in Taipei, Taiwan, and its causes: Implications for ozone control strategies. *Atmos. Environ.* **2006**, *40* (21), 3898−3908; DOI: 10.1016/j.atmosenv.2006.02.018.

(15) Lewis, A. C.; Carslaw, N.; Marriott, P. J.; Kinghorn, R. M.; Morrison, P.; Lee, A. L.; Bartle, K. D.; Pilling, M. J. A larger pool of ozone-forming carbon compounds in urban atmospheres. *Nature* **2000**, *405*, 778−781; DOI: 10.1038/35015546.

(16) Cazorla, M.; Brune, W. H.; Ren, X.; Lefer, B. Direct measurement of ozone production rates in Houston in 2009 and comparison with two estimation methods. *Atmos. Chem. Phys.* **2012**, *12* (2), 1203−1212; DOI: 10.5194/acp-12-1203-2012.

(17) Cazorla, M.; Brune, W. H.; Measurement of ozone production sensor. *Atmos. Meas. Tech.* **2010**, *3* (3), 545−555; DOI: 10.5194/amt-3-545-2010.

(18) Baier, B. C.; Brune, W. M.; Lefer, B. L.; Miller, D. O.; Martins, D. K. Direct ozone production rate measurements and their use in assessing ozone source and receptor regions for Houston in 2013. *Atmos. Environ.* **2015**, *114*, 83−91; DOI: 10.1016/j.atmosenv.2015.05.033.

(19) Fehsenfeld, F. C.; Dickerson, R. R.; Hübler, G.; Luke, W. T.; Nunnermacker, L. J.; Williams, E. J.; Roberts, J. M.; Calvert, J. G.; Curran, C. M.; Delany, A. C.; Eubank, C. S.; Fahey, D. W.; Fried, A.; Gandrud, B. W.; Langford, A. O.; Murphy, P. C.; Norton, R. B.; Pickering, K. E.; Ridley, B. A. A ground-based intercomparison of NO, NO_x, and NO_y measurement techniques. *J. Geophys. Res.* **1987**, *92* (D12), 14710−14722; DOI: 10.1029/JD092iD12p14710.

(20) Burkholder, J. B.; Sander, S. P.; Abbatt, J. P. D.; Barker, J. R.; Huie, R. E.; Kolb, C. E.; Kurylo, M. J.; Orkin, V. L.; Wilmouth, D. M.; Wine, P. H. Chemical Kinetics and Photochemical Data for Use in Atmospheric Studies, Evaluation No. 18. JPL Publication 15-10, Jet Propulsion Laboratory, Pasadena, 2015.

(21) Sadanaga, Y.; Fukumori, Y.; Kobashi, T.; Nagata, M.; Takenaka, N.; Bandow, H. Development of a selective light-emitting diode photolytic NO_2 converter for continuously measuring in the atmosphere. *Anal. Chem.* **2010**, *82* (22), 9234−9239; DOI: 10.1021/ac101703z.

(22) Sadanaga, Y.; Kobashi, T.; Yuba, A.; Kato, S.; Kajii, Y.; Takami, A.; Bandow, H. Evaluation of photochemical production during transport of air pollutants in spring over the East China Sea. *Asian J. Atmos. Environ.* **2015**, *9* (4), 237−246; DOI: 10.5572/ajae.2015.9.4.237.

(23) Kanaya, Y.; Kajii, Y.; Akimoto, H. Solar actinic flux and photolysis frequency determinations by

484 radiometers and a radiative transfer model at Rishiri Island: comparisons, cloud effects, and
485 detection of an aerosol plume from Russian forest fires. *Atmos. Environ.* **2003**, *37* (18),
486 2463−2475; DOI: 10.1016/S1352-2310(03)00183-3.
487 (24) Rohrer, F.; Bohn, B.; Brauers, T.; Brüning, D.; Johnen, F. –J.; Wahner, A.; Kleffmann, J.
488 Characterisation of the photolytic HONO-source in the atmosphere simulation chamber SAPHIR.
489 *Atmos. Chem. Phys.* **2005,** *5,* 2189−2201; DOI: 10.1007/s10874-006-9033-y.
490 (25) Zádor, J.; Turányi, T.; Wirtz, K.; Pilling, M. J. Measurement and investigation of chamber radical
491 source in the European Photoreactor (EUPHORE). *J. Atmos. Chem.* **2006,** *55,* 147−166; DOI:
492 10.5194/acp-5-2189-2005.
493 (26) Sadanaga, Y.; Suzuki, K.; Yoshimoto, T.; Bandow, H. Direct measurement system of nitrogen
494 dioxide in the atmosphere using a blue light emitting diode induced fluorescence technique. *Rev.*
495 *Sci. Instrum.* **2014**, *85* (6), 064101, DOI:10.1063/1.4879821.
496 (27) Ramasamy, S.; Ida, A.; Jones, C.; Kato, S.; Tsurumaru, H.; Kishimoto, I.; Kawasaki, S.; Sadanaga,
497 Y.; Nakashima, Y.; Nakayama, T.; Matsumi, Y.; Mochida, M.; Kagami, S.; Deng, Y.; Ogawa, S.;
498 Kawana, K.; Kajii, Y. Total OH reactivity measurement in a BVOC dominated temperate forest
499 during a summer campaign, 2014. *Atmos. Environ.* **2016**, *131*, 41−54; DOI:
500 10.1016/j.atmosenv.2016.01.039.

501 **Tables**

502 **Table 1** Results from photolysis frequency (unit: s^{-1}) measurements in ambient air, and the reaction and
503 reference chambers

	Ambient*1	Reaction*2	Reference*3	Reac./Amb.*4	Ref./Amb.*5
$J(NO_2)$	9.89×10^{-3}	9.75×10^{-3}	1.20×10^{-3}	0.986	0.121
$J(O_3)$	3.84×10^{-5}	3.95×10^{-5}	~ 0	1.03	~ 0
J(HONO)	1.70×10^{-3}	1.68×10^{-3}	2.84×10^{-5}	0.988	0.017
J(HCHO)	2.75×10^{-5}	2.70×10^{-5}	1.34×10^{-7}	0.984	0.005

504 *1 Photolysis frequencies measured in ambient air.
505 *2 Photolysis frequencies measured in the reaction chamber.
506 *3 Photolysis frequencies measured in the reference chamber.
507 *4 Reaction / Ambient.
508 *5 Reference / Ambient.
509

510

511 **Figure captions**

512 Fig. 1. Schematic diagram of the system for measuring photochemical O_x production rates (MFC =
513 mass flow controller).

514 Fig. 2. Schematic diagram of the reaction chamber. The aluminum flanges are not shown.

515 Fig. 3. Transmission spectra of synthetic quartz plates coated with (a) the clear Teflon and (b) the UV
516 protection films.

517 Fig. 4. Relationship between $[O_3]_{UV}$ and $[NO_2]_{LIF}$. The solid line shows the regression line. Uncertainty
518 in the regression formula was one standard deviation (1σ). Error bars (1σ) of the measured data
519 are within the circles.

520 Fig. 5. Time profiles of $E(\tau)$ in the reaction chamber when (a) "L-shape" and (b) "straight" quartz
521 windows were used for air intake.

522 Fig. 6. Relationship between $[O_3]_{in}$ and $[O_3]_{out}$ in the (a) reaction and (b) reference chambers. Filled and
523 open circles indicate measurements using the chambers with and without the clear Teflon
524 coating, respectively. Solid and dashed lines represent the regression lines for filled and open
525 circles, respectively. Errors are one standard deviation (1σ).

526 Fig. 7. Results of the comparison between $[NO_2]_{in}$ (open bars) and $[NO_2]_{out}$ (gray bars) for the (a)
527 reaction and (b) reference chambers. Error bars are one standard deviation (1σ).

528 Fig. 8. (a) Time series of $P-L(O_x)$ (black line), and $J(NO_2)$ (blue line) measured at WFRS from 5 to 7
529 August, 2014. (b) Time series of $P-L(O_x)$ (black line), O_x (red line) and NO_x mixing ratios
530 (green line) measured at WFRS from 5 to 7 August, 2014.

531

532

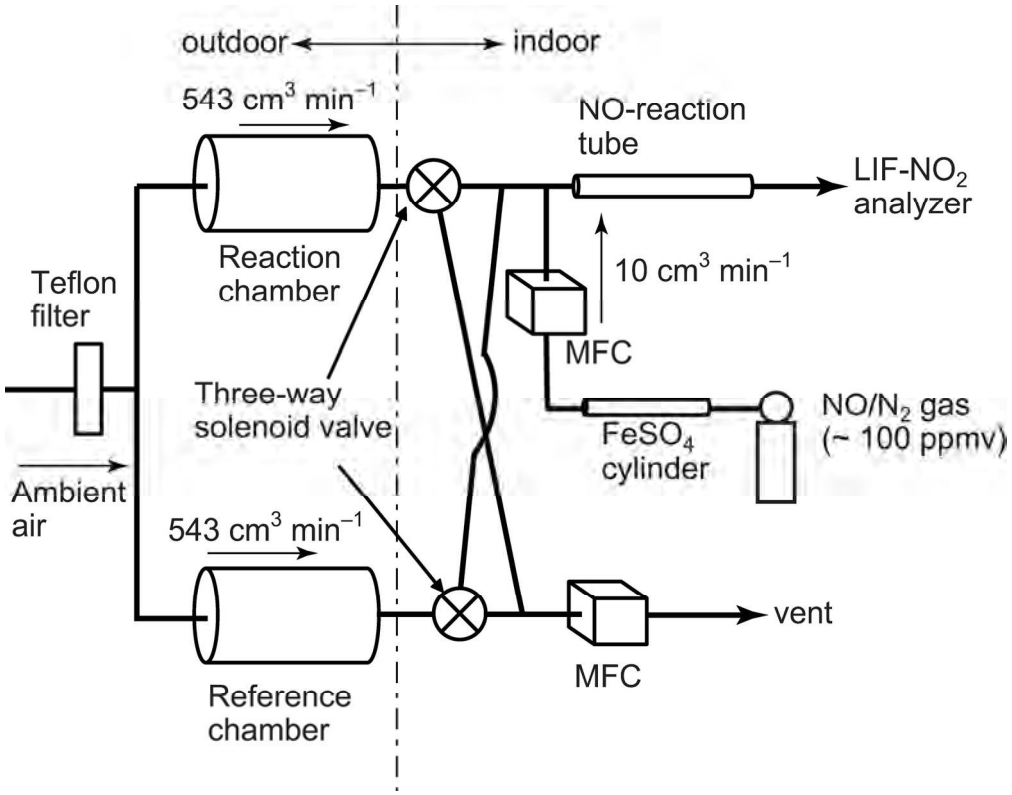

Schematic diagram of the system for measuring photochemical O_x production rates (MFC = mass flow controller).
Figure 1
159x124mm (300 x 300 DPI)

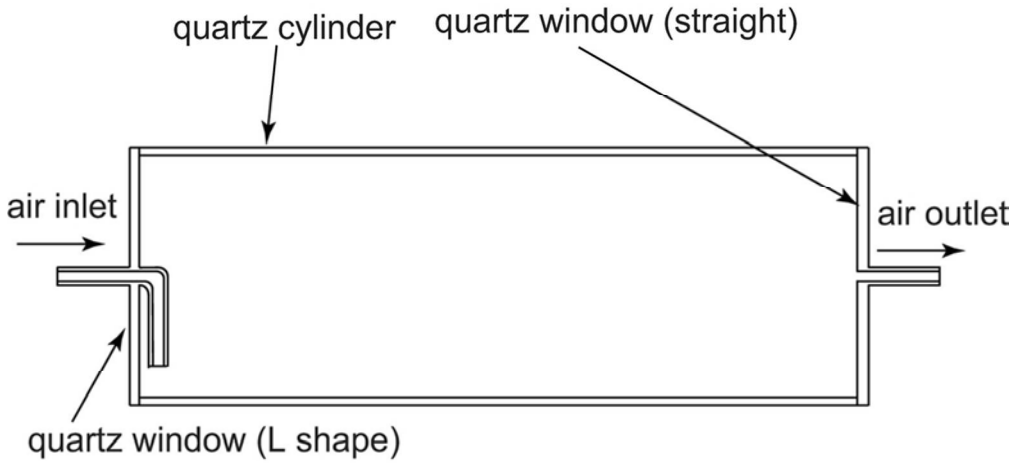

Schematic diagram of the reaction chamber. The aluminum flanges are not shown.
Figure 2
85x39mm (300 x 300 DPI)

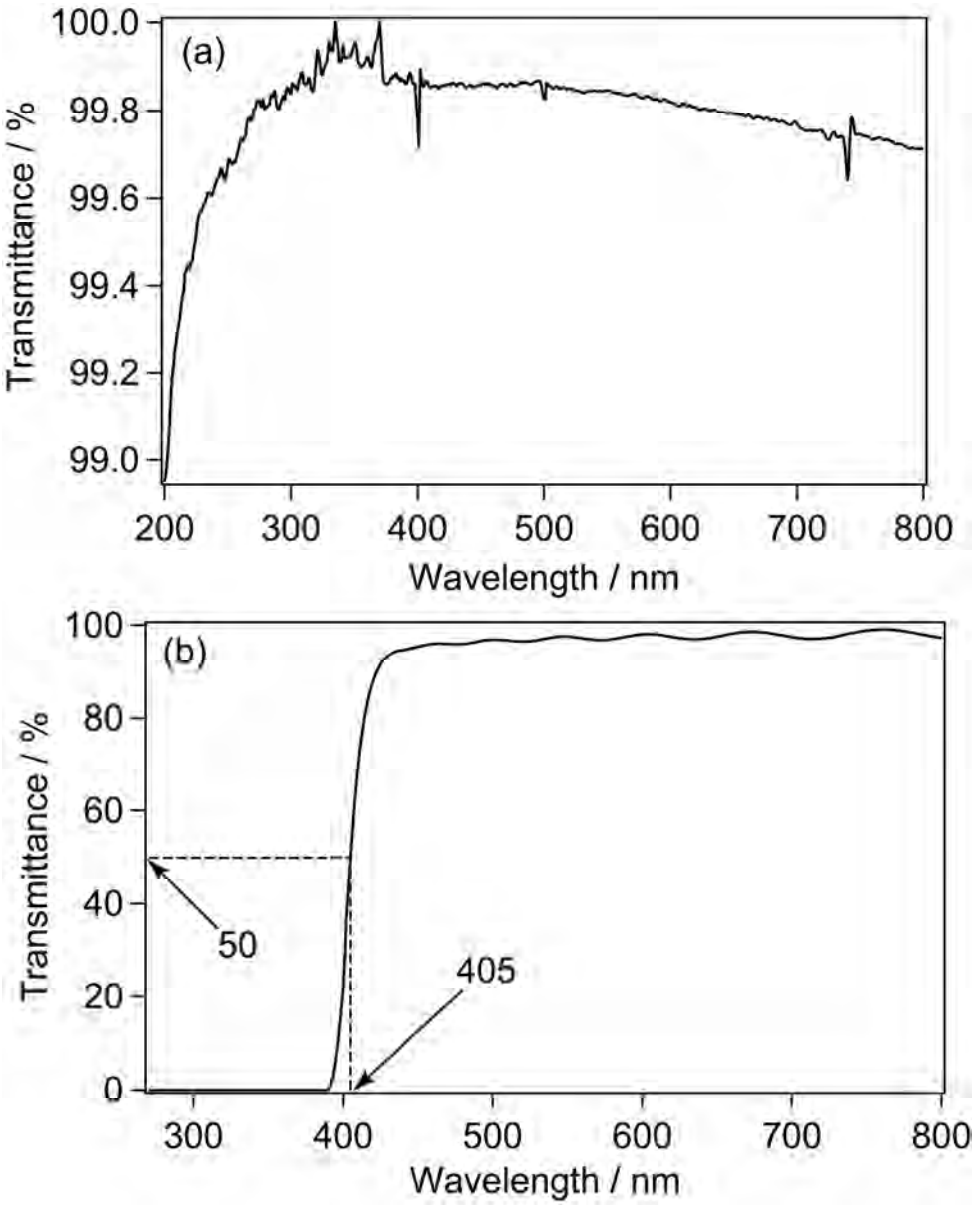

Transmission spectra of synthetic quartz plates coated with (a) the clear Teflon and (b) the UV-cut films.
Figure 3
211x261mm (300 x 300 DPI)

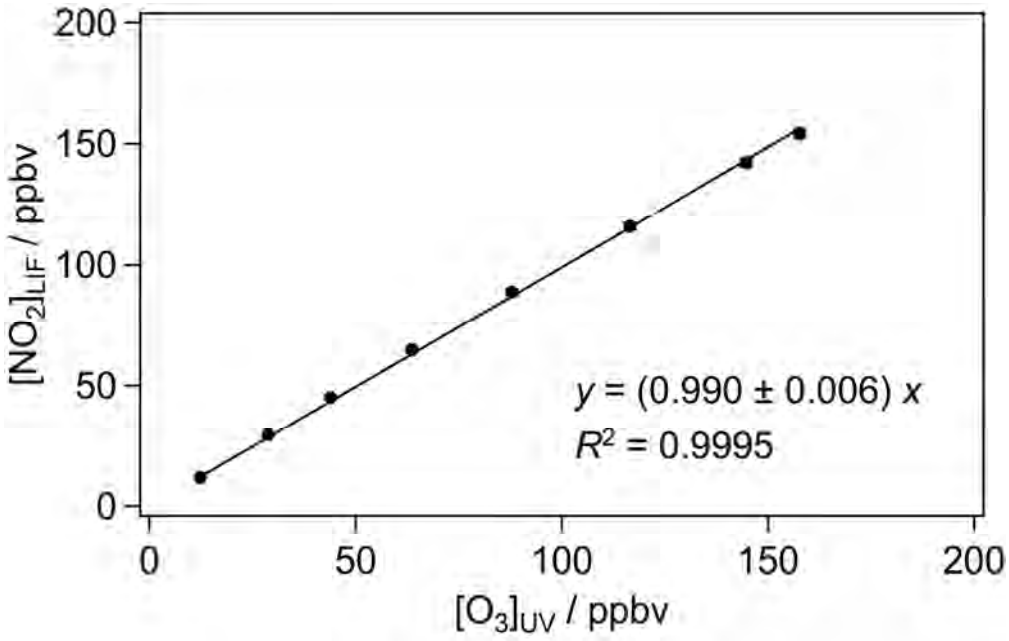

Relationship between $[O_3]_{UV}$ and $[NO_2]_{LIF}$. The solid line shows the regression line. Uncertainty in the regression formula was one standard deviation (1σ). Error bars (1σ) of the measured data are within the circles.
Figure 4
107x68mm (300 x 300 DPI)

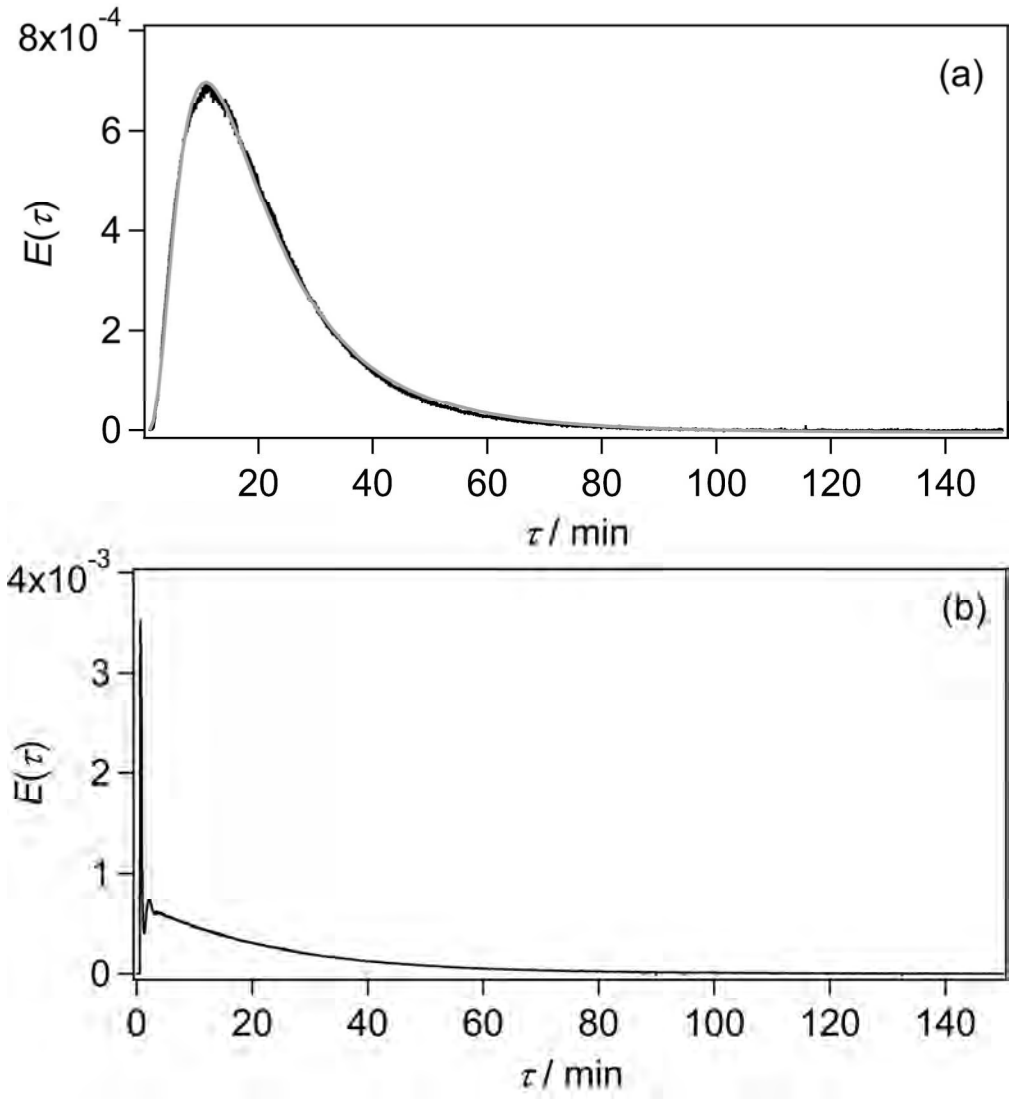

Time profiles of $E(\tau)$ in the reaction chamber when (a) "L-shape" and (b) "straight" quartz windows were used for air intake.

Figure 5

186x204mm (300 x 300 DPI)

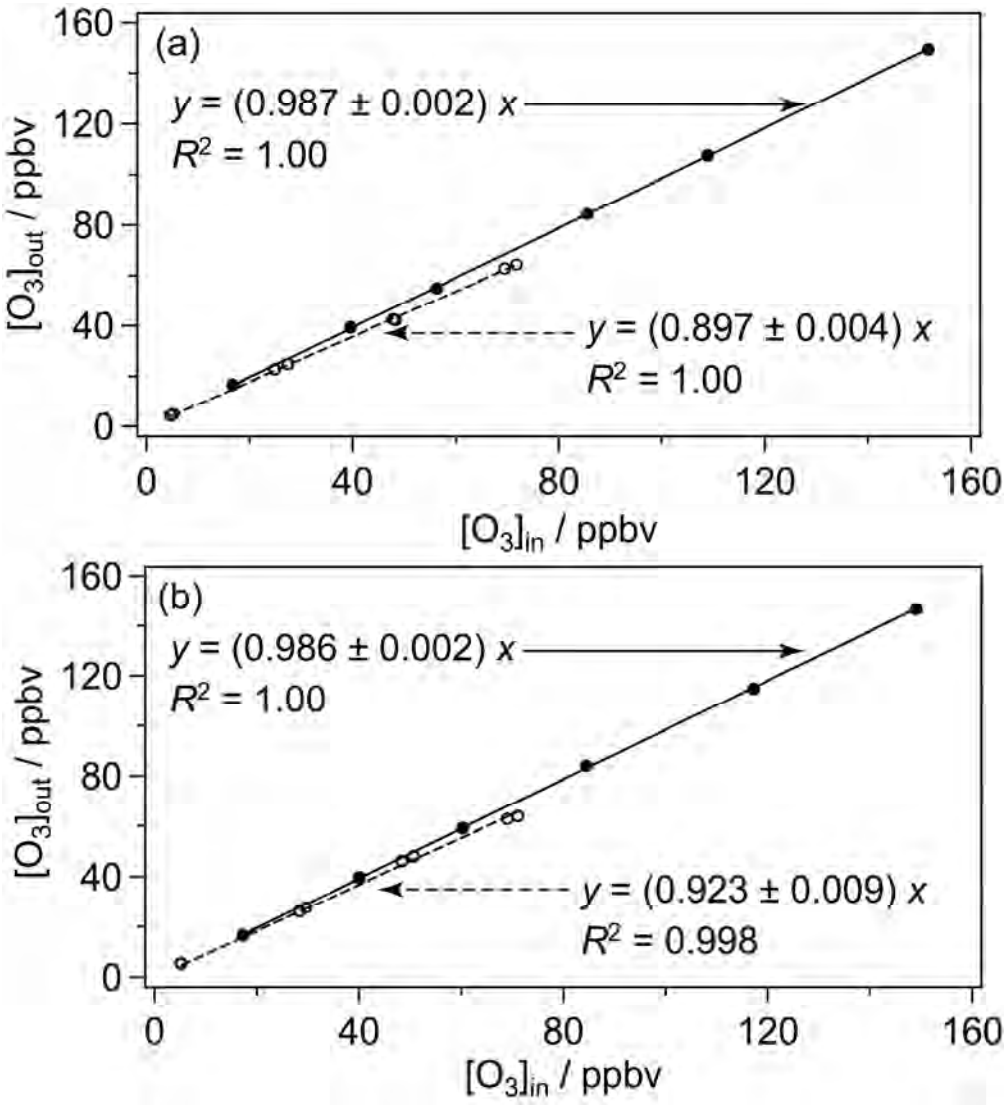

Relationship between $[O_3]_{in}$ and $[O_3]_{out}$ in the (a) reaction and (b) reference chambers. Filled and open circles indicate measurements using the chambers with and without the clear Teflon coating, respectively. Solid and dashed lines represent the regression lines for filled and open circles, respectively. Errors are one standard deviation (1σ).

Figure 6
186x204mm (300 x 300 DPI)

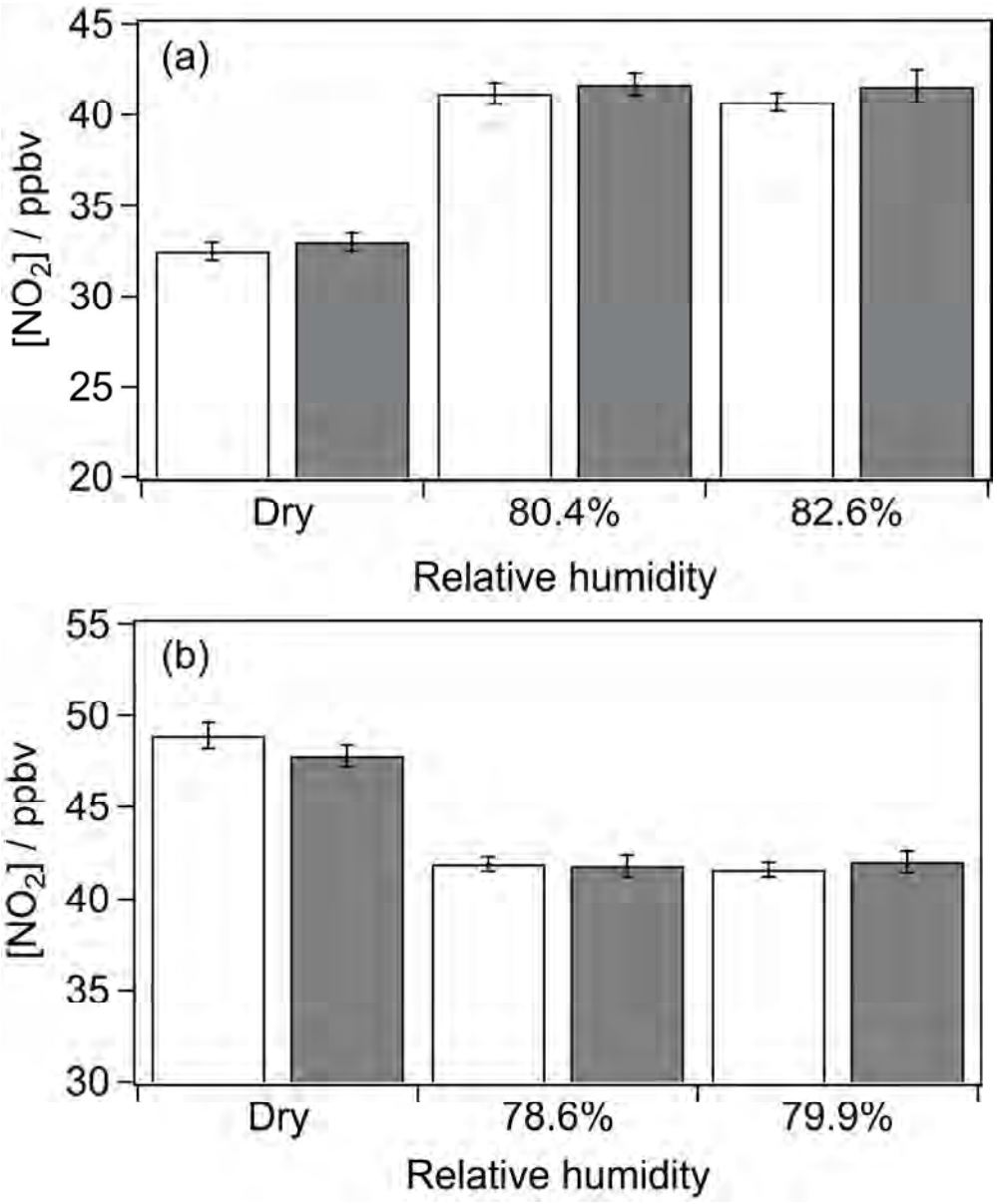

Results of the comparison between $[NO_2]_{in}$ (open bars) and $[NO_2]_{out}$ (gray bars) for the (a) reaction and (b) reference chambers. Error bars are one standard deviation (1σ).

Figure 7

190x230mm (300 x 300 DPI)

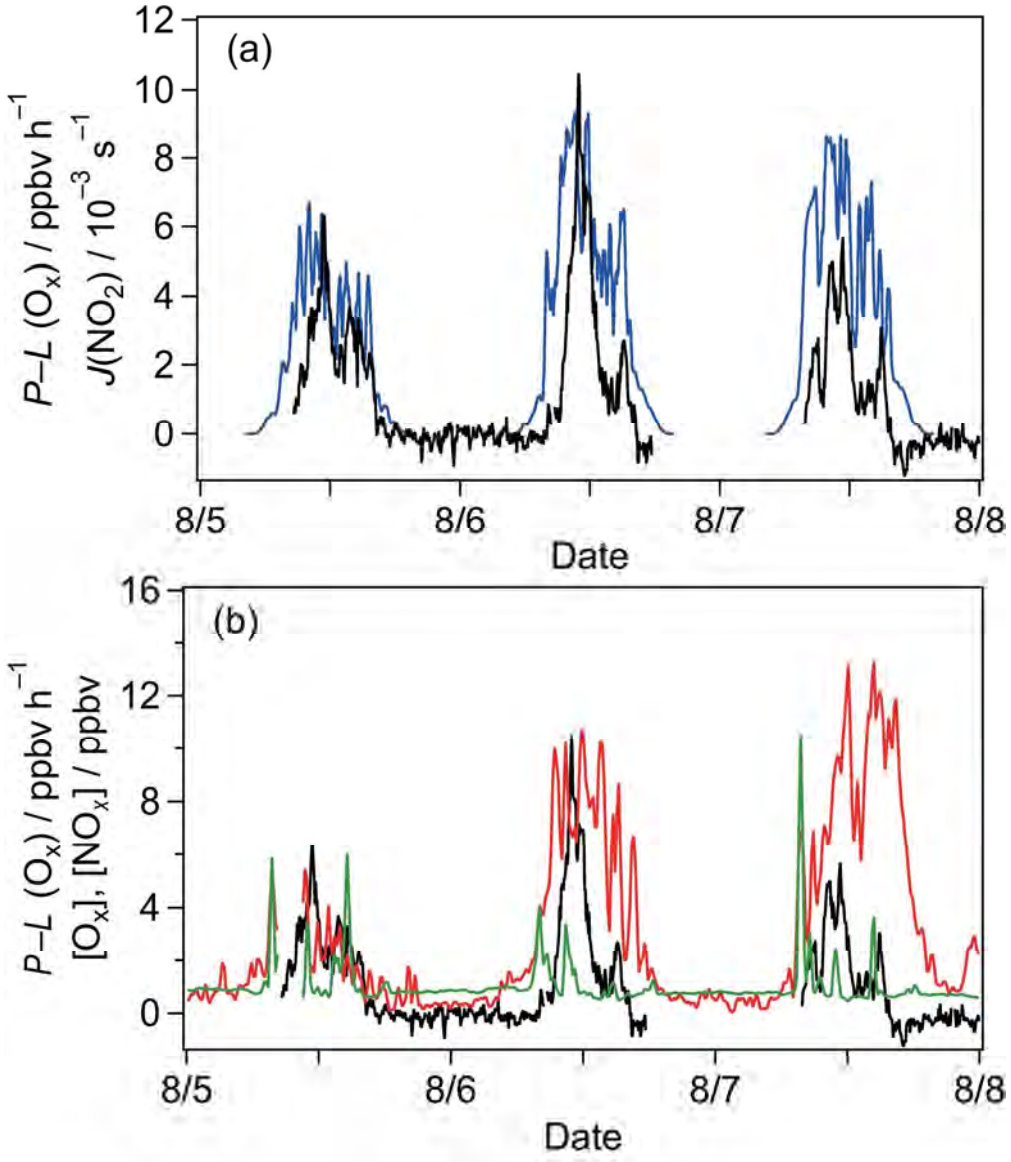

(a) Time series of P−L(O_x) (black line), and J(NO_2) (blue line) measured at WFRS from 5 to 7 August, 2014.
(b) Time series of P−L(O_x) (black line), O_x (red line) and NO_x mixing ratios (green line) measured at WFRS from 5 to 7 August, 2014.
Figure 8
196x228mm (300 x 300 DPI)